

J2229+2725: an extremely low-metallicity dwarf compact star-forming galaxy with an exceptionally high [O III] λ 5007/[O II] λ 3727 flux ratio of 53

Y. I. Izotov^{1*}, T. X. Thuan² and N. G. Guseva¹

¹*Bogolyubov Institute for Theoretical Physics, National Academy of Sciences of Ukraine, 14-b Metrolohichna str., Kyiv, 03143, Ukraine,*

²*Astronomy Department, University of Virginia, P.O. Box 400325, Charlottesville, VA 22904-4325,*

19 April 2021

ABSTRACT

Using the Large Binocular Telescope (LBT)/Multi-Object Dual Spectrograph (MODS), we have obtained optical spectroscopy of one of the most metal-poor dwarf star-forming galaxies (SFG) in the local Universe, J2229+2725. This galaxy with a redshift $z=0.0762$ was selected from the Data Release 16 (DR16) of the Sloan Digital Sky Survey (SDSS). Its properties derived from the LBT observations are most extreme among SFGs in several ways. Its oxygen abundance $12 + \log\text{O}/\text{H} = 7.085 \pm 0.031$ is among the lowest ever observed for a SFG. With its very low metallicity, an absolute magnitude $M_g = -16.39$ mag, a low stellar mass $M_* = 9.1 \times 10^6 M_\odot$ and a very low mass-to-light ratio $M_*/L_g \sim 0.0166$ (in solar units), J2229+2725 deviates strongly from the luminosity-metallicity relation defined by the bulk of the SFGs in the SDSS. J2229+2725 has a very high specific star-formation rate $\text{sSFR} \sim 75 \text{ Gyr}^{-1}$, indicating very active ongoing star formation. Three other features of J2229+2725 are most striking, being the most extreme among lowest-metallicity SFGs: 1) a ratio $\text{O}_{32} = I([\text{O III}]\lambda 5007)/I([\text{O II}]\lambda 3727) \sim 53$, 2) an equivalent width of the $\text{H}\beta$ emission line $\text{EW}(\text{H}\beta)$ of 577 \AA , and 3) an electron number density of $\sim 1000 \text{ cm}^{-3}$. These properties imply that the starburst in J2229+2725 is very young. Using the extremely high O_{32} in J2229+2725, we have improved the strong-line calibration for the determination of oxygen abundances in the most metal-deficient galaxies, in the range $12 + \log\text{O}/\text{H} \lesssim 7.3$.

Key words: galaxies: dwarf – galaxies: starburst – galaxies: ISM – galaxies: abundances.

1 INTRODUCTION

Extremely metal-deficient (XMD) low-redshift star-forming galaxies (SFGs), with oxygen abundances as low as $12 + \log\text{O}/\text{H} \sim 6.9 - 7.1$ have been recently uncovered in a number of studies. Thus, Hirschauer et al. (2016) have reported $12 + \log\text{O}/\text{H} = 7.02 \pm 0.03$ in the galaxy AGC 198691. Hsyu et al. (2017) have found the oxygen abundance in the galaxy Little Cub to be $12 + \log\text{O}/\text{H} = 7.13 \pm 0.08$. Izotov et al. (2018a) and Izotov et al. (2019a), based on Large Binocular Telescope (LBT) observations, derived oxygen abundances in J0811+4730 and J1234+3901 of 6.98 ± 0.02 and 7.035 ± 0.026 , respectively. Both these galaxies have been selected from the Sloan Digital Sky Survey (SDSS). Kojima et al. (2020) have recently reported the

discovery of the galaxy J1631+4426 with $12 + \log\text{O}/\text{H} = 6.90 \pm 0.03$. In all these studies, the oxygen abundances have been derived by the direct T_e method from spectra of the entire galaxy. The common characteristics of the galaxies mentioned above are their low stellar mass $M_* \lesssim 10^7 M_\odot$ and a very compact structure. Besides these galaxies, very low oxygen abundances of 7.01 ± 0.07 , 6.98 ± 0.06 , 6.86 ± 0.14 have also been found by Izotov et al. (2009) in three individual H II regions of the XMD SBS 0335–052W. The value of 6.96 ± 0.09 has been obtained by Annibali et al. (2019) in one of the H II regions in the dwarf irregular galaxy DDO 68. However, some other regions in SBS 0335–052W and DDO 68 show oxygen abundances above 7.1.

The importance of finding and studying these galaxies is emphasized by the fact that they share many of the same properties with the dwarf galaxies at high redshifts and thus may be considered as the their best local

* Corresponding author: yizotov@bitp.kiev.ua

counterparts. Therefore, the low-redshift XMD SFGs with $12 + \log O/H \sim 7.0$ are excellent laboratories for studying the physical conditions in dwarf galaxies at redshifts $z \sim 5$ – 10 , during the epoch of the Universe’s reionisation.

In this paper, we present LBT¹ spectroscopic observations of a new SFG, J2229+2725. The galaxy was selected from the SDSS Data Release 16 (DR16) data base (Ahumada et al. 2020) as a candidate to be an extremely low-metallicity object, using criteria such as the simultaneous presence of a low $[O\ III]\lambda 5007/H\beta$ ratio of $\lesssim 3$ and of a weak or undetected $[N\ II]\lambda 6584$ emission line with a flux $\lesssim 1/100$ that of the $H\alpha$ emission line (e.g. Izotov et al. 2019b). We also selected J2229+2725 because of its extremely high O_{32} value, defined as the ratio $I([O\ III]\lambda 5007)/I([O\ II]\lambda 3727)$. This high ratio implies that the galaxy may contain density-bounded H II regions, and thus be a potential Lyman continuum leaker (e.g. Jaskot & Oey 2013) and a good local counterpart to the high-redshift dwarf galaxies thought to be responsible for the reionisation of the early Universe (Ouchi et al. 2009; Wise & Chen 2009; Yajima, Choi & Nagamine 2011; Mitra, Ferrara & Choudhury 2013; Bouwens et al. 2015; Izotov et al. 2016a,b, 2018b,c). Its coordinates, redshift and other characteristics obtained from the photometric and spectroscopic SDSS, the *Galaxy Evolution Explorer* (*GALEX*) and LBT data are presented in Table 1. The SDSS image of J2229+2725 is displayed in Fig. 1. For comparison, we show the round 2 arcsec SDSS spectroscopic aperture centered on the galaxy and the 1.2 arcsec wide LBT slit. The galaxy is very compact, with a full width at half maximum (FWHM) of 0.9 arcsec, comparable to the median Apache Point Observatory (APO) and LBT Observatory (LBTO) seeings during the observations and corresponding to a linear size of 1.3 kpc. The actual size of J2229+2725 is likely smaller and comparable to the sub-kpc sizes of compact star-forming galaxies at similar redshifts with $O_{32} = 22 - 39$, observed with the *Hubble Space Telescope* (*HST*) (Izotov et al. 2020). No substantial emission from J2229+2725 is seen outside the SDSS spectroscopic aperture and the LBT slit in Fig. 1, implying that aperture corrections are small.

2 OBSERVATIONS AND DATA REDUCTION

We have obtained LBT long-slit spectrophotometric observations of J2229+2725 on 15 September, 2020 in the twin binocular mode, using the MODS1 and MODS2 spectrographs². The night was nearly clear with some small clouds

¹ The LBT is an international collaboration among institutions in the United States, Italy and Germany. LBT Corporation partners are: The University of Arizona on behalf of the Arizona university system; Istituto Nazionale di Astrofisica, Italy; LBT Beteiligungsgesellschaft, Germany, representing the Max-Planck Society, the Astrophysical Institute Potsdam, and Heidelberg University; The Ohio State University, and The Research Corporation, on behalf of The University of Notre Dame, University of Minnesota and University of Virginia.

² This paper used data obtained with the MODS spectrographs built with funding from NSF grant AST-9987045 and the NSF Telescope System Instrumentation Program (TSIP), with additional funds from the Ohio Board of Regents and the Ohio State University Office of Research.

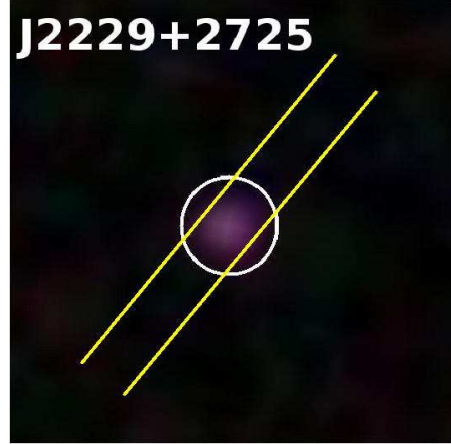


Figure 1. 12 arcsec \times 12 arcsec region with the color composite SDSS image of J2229+2725. The 2 arcsec SDSS spectroscopic aperture and 1.2 arcsec wide LBT/MODS slit are indicated by a white circle and yellow parallel lines, respectively.

Table 1. Observed and derived characteristics of J2229+2725

Parameter	J2229+2725
R.A.(J2000)	22:29:33.19
Dec.(J2000)	+27:25:25.60
z	0.07622
<i>GALEX</i> FUV, mag	21.45 \pm 0.28
<i>GALEX</i> NUV, mag	21.88 \pm 0.37
SDSS <i>u</i> , mag	21.96 \pm 0.15
SDSS <i>g</i> , mag	21.47 \pm 0.04
SDSS <i>r</i> , mag	22.27 \pm 0.11
SDSS <i>i</i> , mag	20.97 \pm 0.05
SDSS <i>z</i> , mag	21.43 \pm 0.33
D_L , Mpc*	347
M_g , mag [†]	-16.39 \pm 0.06
$\log L_g/L_{g,\odot}$ [‡]	8.74
$\log M_*/M_\odot$ ^{††}	6.96
M_*/L_g , $M_\odot/L_{g,\odot}$	0.0166
$L(H\beta)$, erg s ^{-1**}	(3.1 \pm 0.3) $\times 10^{40}$
SFR, M_\odot yr ^{-1†††}	0.68 \pm 0.06
sSFR, Gyr ⁻¹	75
$12 + \log O/H$ ^{††††}	7.085 \pm 0.031

*Luminosity distance.

[†]Absolute magnitude corrected for Milky Way extinction.

[‡] \log of the SDSS *g*-band luminosity corrected for Milky Way extinction.

^{††}Stellar mass derived from the extinction-corrected SDSS spectrum.

** $H\beta$ luminosity derived from the extinction-corrected SDSS spectrum.

^{†††}Star formation rate derived from the Kennicutt (1998) relation using the extinction-corrected $H\beta$ luminosity.

^{††††}Oxygen abundance derived from the LBT spectrum.

moving through. Spectra were obtained in the wavelength range 3200 – 10000Å with a 1.2 arcsec wide slit, resulting in a resolving power $R \sim 2000$. The seeing during the observations was 1.0 arcsec.

Four 900 s subexposures were obtained in both the blue and red ranges separately with MODS1 and MODS2, resulting in a total exposure time of 2×3600 s, counting both spectrographs. The airmass during observations was small,

Table 2. Extinction-corrected emission-line flux ratios*

Line	J2229+2725
3721.94 H14	1.43±0.21
3727.00 [O II]	5.72±0.39
3734.37 H13	2.63±0.38
3750.15 H12	4.45±0.59
3770.63 H11	5.22±0.61
3797.90 H10	6.36±0.54
3819.64 He I	1.52±0.24
3835.39 H9	7.35±0.54
3868.76 [Ne III]	22.49±0.81
3889.00 He I+H8	19.97±0.84
3968.00 [Ne III]+H7	23.81±0.92
4026.19 He I	1.95±0.32
4101.74 H δ	26.34±0.97
4227.20 [Fe V]	1.35±0.21
4340.47 H γ	46.57±1.48
4363.21 [O III]	13.96±0.56
4471.48 He I	3.92±0.28
4685.94 He II	2.12±0.24
4712.00 [Ar IV]+He I	2.85±0.25
4740.20 [Ar IV]	1.89±0.22
4861.33 H β	100.00±2.97
4921.93 He I	1.60±0.21
4958.92 [O III]	100.01±2.96
5006.80 [O III]	300.36±8.79
5875.60 He I	9.47±0.31
6312.10 [S II]	0.36±0.12
6562.80 H α	269.65±8.50
6583.40 [N II]	0.26±0.12
6678.10 He I	2.31±0.12
6716.40 [S II]	0.56±0.06
6730.80 [S II]	0.62±0.06
7065.30 He I	4.51±0.27
7135.80 [Ar III]	0.79±0.08
7281.35 He I	0.79±0.06
<hr/>	
$C(H\beta)^\dagger$	0.060±0.038
$F(H\beta)^\ddagger$	21.45±0.12
EW(H β)**	577.2±3.6
EW(abs)**	3.4±1.1

*in units $100 \times I(\lambda)/I(H\beta)$. † Extinction coefficient, derived from the observed hydrogen Balmer decrement. ‡ Observed flux in units of 10^{-16} erg s $^{-1}$ cm $^{-2}$.

**Equivalent width in Å.

it is offset to low R_{23} compared to the main sequence defined by the SDSS SFGs, due to its extremely low oxygen abundance. Second, the H β equivalent width EW(H β) of ~ 577 Å is also enormous. Both features indicate that the starburst in J2229+2725 is very young, with an age $\lesssim 1 - 2$ Myr. Its spectrum shows a relatively strong He II $\lambda 4686$ emission line, with a flux ~ 2.1 per cent that of the H β emission line, similar to that in integrated spectra of other lowest-metallicity compact star-forming galaxies (e.g. in J0811+4730 and J1234+3901, Izotov et al. 2018a, 2019a) and indicative of the presence of hard ionising radiation.

3 HEAVY ELEMENT ABUNDANCES

We use here the emission-line fluxes derived from the LBT spectrum to derive heavy element abundances. We empha-

Table 3. Electron temperatures, electron number density and heavy element abundances

Property	J2229+2725
$T_e(O III)$, K	24800±900
$T_e(O II)$, K	16000±400
$T_e(S III)$, K	20800±700
$N_e(S II)$, cm $^{-3}$	1000±600
<hr/>	
$O^+/H^+ \times 10^6$	0.472±0.044
$O^{2+}/H^+ \times 10^5$	1.138±0.087
$O^{3+}/H^+ \times 10^6$	0.319±0.046
$O/H \times 10^5$	1.218±0.087
$12+\log(O/H)$	7.085±0.031
<hr/>	
$N^+/H^+ \times 10^7$	0.196±0.071
ICF(N)	18.304
$N/H \times 10^7$	3.584±1.467
$\log(N/O)$	-1.535±0.180
<hr/>	
$Ne^{2+}/H^+ \times 10^6$	1.805±0.130
ICF(Ne)	1.029
$Ne/H \times 10^6$	1.856±0.139
$\log(Ne/O)$	-0.817±0.045
<hr/>	
$S^+/H^+ \times 10^7$	0.129±0.013
$S^{2+}/H^+ \times 10^7$	0.768±0.260
ICF(S)	3.844
$\log(S/O)$	-1.552±0.130
<hr/>	
$Ar^{2+}/H^+ \times 10^7$	0.191±0.021
ICF(Ar)	2.162
$Ar/H \times 10^7$	0.413±0.173
$\log(Ar/O)$	-2.469±0.185

size that the LBT spectrum is crucial for this task as some important lines, such as the [O III] λ 5007 and the H α lines, are clipped in the SDSS spectrum. We follow the prescriptions of Izotov et al. (2006) to derive heavy element abundances in J2229+2725. The electron temperature $T_e(O III)$ is calculated from the [O III] λ 4363/(λ 4959 + λ 5007) emission-line flux ratio. It is used to derive the abundances of O^{3+} , O^{2+} and Ne^{2+} . The [S III] λ 9069 and [O II] λ 7320, 7330 emission lines, which can, in principle, be used to directly derive the temperatures, are not detected in the LBT spectrum of J2229+2725. Therefore, the abundances of O^+ , N^+ and S^+ are derived with the electron temperature $T_e(O II)$ and the abundances of S^{2+} and Ar^{2+} are derived with the electron temperature $T_e(S III)$, using the relations of Izotov et al. (2006) between $T_e(O II)$, $T_e(S III)$ and $T_e(O III)$. The electron number density was derived from the [S II] λ 6717/ λ 6731 flux ratio. The electron temperatures and electron number densities are shown in Table 3. We note that the electron temperature $T_e(O III)$ of 24,800 K is very high, implying that the oxygen abundance is low. Furthermore, the number density of the ionised gas is also very high, equal to 1000 cm $^{-3}$, which is atypical of SFGs, indicating a very young age for the star-forming region.

The ionic abundances, ionisation correction factors and total O, N, Ne, S and Ar abundances are obtained using relations by Izotov et al. (2006). They are presented in Table 3.

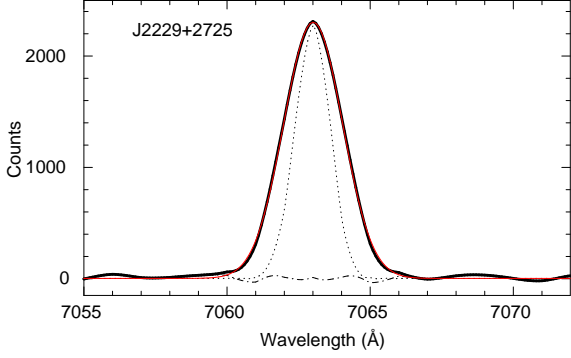


Figure 3. The $H\alpha$ profile in the medium-resolution DIS spectrum of J2229+2725. The observed spectrum is shown by a black solid line while the Gaussian fit is represented by a red solid line. The black dash-dotted line shows the residual spectrum after subtraction of the $H\alpha$ fit. The instrumental profile is represented by a black dotted line.

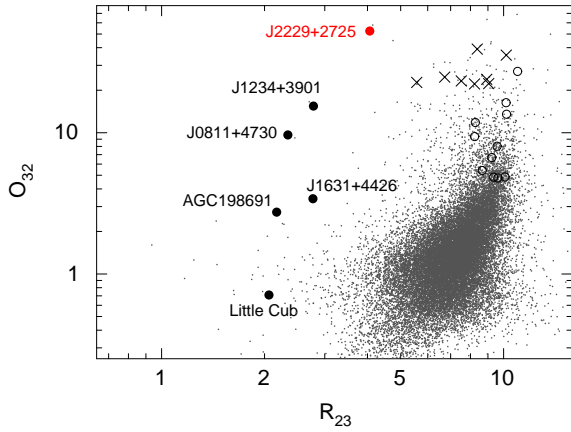


Figure 4. The $O_{32} - R_{23}$ diagram for compact SFGs, where $O_{32} = I([\text{O III}]\lambda 5007)/I([\text{O II}]\lambda 3727)$ and $R_{23} = I([\text{O II}]\lambda 3727 + [\text{O III}]\lambda 4959 + [\text{O III}]\lambda 5007)/I(H\beta)$. The lowest-metallicity SFGs known with $12 + \log \text{O}/\text{H} < 7.1$ from Hirschauer et al. (2016, A198691), Hsyu et al. (2017, Little Cub), Izotov et al. (2018a, J0811+4730), Izotov et al. (2019a, J1234+3901), Kojima et al. (2020, J1631+4426) and this paper (J2229+2725) are shown by labelled filled circles. LyC leakers from Izotov et al. (2016a,b, 2018b,c) are shown by open circles. SFGs with the highest O_{32} from Izotov et al. (2020) are represented by crosses and compact SFGs from the SDSS DR16 by grey dots.

The nebular oxygen abundance of $12 + \log \text{O}/\text{H} = 7.085 \pm 0.031$ in J2229+2725 is among the lowest found for SFGs, where $\text{O}/\text{H} = \text{O}^+/\text{H}^+ + \text{O}^{2+}/\text{H}^+ + \text{O}^{3+}/\text{H}^+$. The N/O, Ne/O, S/O and Ar/O abundance ratios for this galaxy are similar to those in other low-metallicity SFGs (e.g., Izotov et al. 2006).

4 KINEMATICS OF THE IONISED GAS

The medium-resolution DIS spectrum allows us to put constraints on the kinematics of ionised gas in J2229+2725. In Fig. 3 is shown the $H\alpha$ profile at observed wavelengths (black solid line). It is somewhat broader than the instrumental profile shown by a black dotted line. Thus, the $H\alpha$

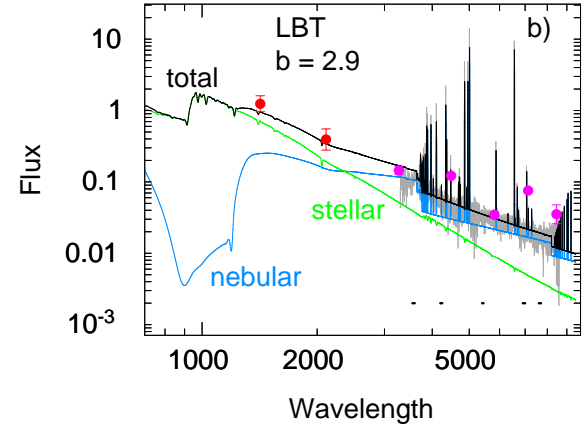
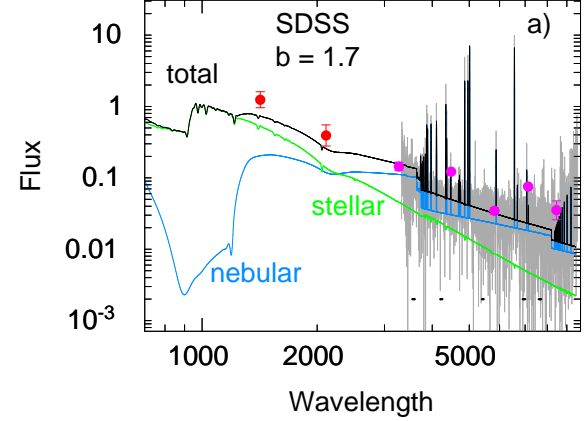


Figure 5. a) and b) Best-fit spectral energy distributions obtained from fitting the rest-frame SDSS and LBT spectra, respectively, by randomly varying t_b , t_1 , t_2 and $b = M_{\text{old}}/M_{\text{young}}$, where t_b is the age of young stellar population, $t_2 - t_1$ is the interval, in which the old stellar population was formed. In both panels, the observed spectra are shown in grey, the modelled stellar, nebular and total SEDs are shown by green, blue and black lines, respectively, and are labelled. *GALEX* FUV, NUV and SDSS u , g , r , i and z photometric data, blueshifted adopting the J2229+2725 redshift, are shown by red and magenta filled circles, respectively. Short horizontal lines represent intervals used for continuum fitting, which are free of emission lines. Fluxes are in units 10^{-16} erg $\text{s}^{-1} \text{cm}^{-2} \text{\AA}^{-1}$ and wavelengths are in \AA .

emission line is partially resolved. Its profile is perfectly fitted by a single Gaussian profile (red solid line), indicating a simple kinematical structure of the ionised gas with a regular motion, characteristic of a single H II region without evident signs of merging or asymmetric infall or outflow.

Using the relation

$$\sigma_{\text{int}} = \frac{\sqrt{FWHM_{\text{obs}}^2 - FWHM_{\text{inst}}^2}}{2.355} \frac{300000}{\lambda_{\text{obs}}} \text{ km s}^{-1} \quad (1)$$

we deconvolve the observed $H\alpha$ profile with the instrumental profile and derive an intrinsic velocity dispersion σ_{int} . Here $FWHM_{\text{obs}}$ and $FWHM_{\text{inst}}$ are the measured full widths at half maximum of the $H\alpha$ and instrumental profiles at observed wavelength λ_{obs} . We derive an intrinsic velocity dispersion $\sigma_{\text{int}} = 34.7 \text{ km s}^{-1}$. The intrinsic velocity dispersion consists of the thermal and turbulent components. Adopting

the electron temperature $T_e(\text{O III}) = 24800 \text{ K}$ (Table 3) and the relation

$$\sigma_{\text{th}} = \sqrt{\frac{kT_e(\text{O III})}{m}} \quad (2)$$

we obtain the thermal velocity dispersion for hydrogen atoms $\sigma_{\text{th}} = 14.3 \text{ km s}^{-1}$. In Eq. 2, k is the Boltzman constant, m is the proton mass. Finally, deconvolving the intrinsic profile with a thermal profile

$$\sigma_{\text{tur}} = \sqrt{\sigma_{\text{int}}^2 - \sigma_{\text{th}}^2}, \quad (3)$$

we obtain the velocity dispersion for the turbulent component $\sigma_{\text{tur}} = 31.6 \text{ km s}^{-1}$.

Thus, the broadening of the $\text{H}\alpha$ emission line in J2229+2725 is dominated by macroscopic turbulent motions.

5 INTEGRATED CHARACTERISTICS OF J2229+2725

Everywhere in the paper, we have adopted the luminosity distance $D_L = 347 \text{ Mpc}$, obtained from the galaxy redshift for the cosmological parameters $H_0 = 67.1 \text{ km s}^{-1} \text{ Mpc}^{-1}$, $\Omega_m = 0.318$, $\Omega_\Lambda = 0.682$ (Planck Collaboration XVI 2014). It is used to derive integrated characteristics such as stellar mass and luminosities.

The stellar mass of J2229+2725 is determined from fitting the spectral energy distribution (SED). We follow the prescriptions of Izotov et al. (2018a), STARBURST99 models (Leitherer et al. 1999) and adopt stellar evolution models by Girardi et al. (2000), stellar atmosphere models by Lejeune, Buser & Cuisiner (1997) and the Salpeter (1955) initial mass function (IMF) with lower and upper mass limits of $0.1 M_\odot$ and $100 M_\odot$, respectively.

The equivalent width of the $\text{H}\beta$ emission line in J2229+2725 of 577 \AA is exceptionally high (Table 2), indicating a very high contribution of the nebular continuum, amounting to more than 50 per cent of the total continuum near the $\text{H}\beta$ emission line. Therefore, following e.g. Izotov et al. (2018a), both the stellar and nebular continua are taken into account in the SED fitting. The star-formation history in J2229+2725 was approximated by a recent short burst at age $t_b < 10 \text{ Myr}$ and a prior continuous star formation with a constant SFR during the time interval $t_2 - t_1$ with $t_1, t_2 > 10 \text{ Myr}$ and $t_2 > t_1$. We use a Monte Carlo method with χ^2 minimisation, varying t_b, t_1, t_2 and the mass fraction of stellar populations $b = M_{\text{old}}/M_{\text{young}}$ formed after the age of 10 Myr and during the burst, and aiming to obtain the best agreement between the modelled and observed continuum over the entire wavelength range of the SDSS spectrum. Additionally, the observed $\text{EW}(\text{H}\beta)$ and $\text{EW}(\text{H}\alpha)$ have to be simultaneously reproduced by the best model. More details on the SED fitting procedure can be found e.g. in Izotov et al. (2018a).

We use both the continua of SDSS and LBT spectra, avoiding regions with emission lines, to fit SEDs and to derive stellar masses. The best fits are shown in Fig. 5a for the SDSS spectrum and in Fig. 5b for the LBT spectrum. It is clear that the LBT spectrum has a considerably better signal to noise ratio than the SDSS spectrum. Thus, the physical parameters derived from the LBT data are more reliable,

and we shall adopt them throughout the paper. However, we discuss also in this section the parameters derived from the SDSS spectrum for comparison.

The derived parameters t_b, t_1, t_2, b and stellar masses $M_{\text{young}}, M_{\text{old}}$ and $M_* = M_{\text{young}} + M_{\text{old}}$ of the SED fits are presented in Table 4 (second column is for the SDSS spectrum and fifth column is for the LBT spectrum). We note that the photometric SDSS and GALEX data are not used for SED fitting. The SDSS photometric fluxes (magenta symbols in Fig. 5) are derived from model magnitudes extracted from the SDSS data base. The model magnitudes are calculated using the best-fit parameters of the galaxy brightness profile in the r band, and applying them to all other bands; the light is therefore measured consistently through the same aperture in all bands. These magnitudes are very similar to the PSF magnitudes presented in the same data base. The SDSS photometric fluxes in g, i and z bands are considerably higher than the fluxes in the continuum at the same wavelengths, due to the contribution of strong emission lines, whereas the contribution of emission lines in the u and r bands is small. The fluxes in GALEX FUV and NUV photometric bands can be used to check the quality of SED fitting in the UV range. It is seen in Fig. 5a that observed FUV and NUV fluxes (red symbols) are slightly above the fluxes modelled with the SDSS spectrum (black line), whereas the agreement is much better for the fit to the LBT spectrum (Fig. 5b).

The remarkable feature of J2229+2725 is that the continuum in the visible range is dominated by nebular emission (blue line in Fig. 5), which is several times higher than the stellar emission (green line in Fig. 5). Its contribution to the total emission in the continuum increases with increasing wavelength. Nebular emission in this galaxy is considerable even in the UV range longward of the $\text{Ly}\alpha$ line, due to sharply rising two-photon emission at $\lambda \geq 1215.67 \text{ \AA}$. It should be taken into account e.g. in the determination of the UV stellar slope β , commonly used in studies of star-forming galaxies.

The mass of the young stellar population M_{young} of $\sim 10^{6.4} M_\odot$ is consistently derived from both the SDSS and LBT spectra (Table 4), despite the fact that the SDSS spectrum is considerably noisier (compare Fig. 5a and 5b). The determination of the mass of old stellar population M_{old} is much more uncertain because of its negligible contribution to emission in the visible range. We obtain a stellar mass for J2229+2725 as low as $M_* = 10^{6.96} M_\odot$ from the best-fit SED to the LBT spectrum (Table 4). This yields a very high specific star formation rate sSFR of $\sim 75 \text{ Gyr}^{-1}$, indicative of very active ongoing star formation.

For the sake of comparison, we also derive best-fit SEDs adopting $b = 0$, corresponding to $M_{\text{old}} = 0$, with parameters presented in the third and sixth columns of Table 4. In this case we derive the lower stellar mass limit $M_* = M_{\text{young}} \sim 10^{6.3} M_\odot$.

On the other hand, assuming that the old stellar population consists only of the least luminous stars in the age range of $\sim 10 - 13 \text{ Gyr}$, we can set an upper limit for the total stellar mass M_* . For J2229+2725 it can not be higher than $\sim 10^{7.3} M_\odot$, corresponding to $b \sim 8$ (see the other parameters for the best-fit models with $b = 8$ in columns four and seven of Table 4). Otherwise, the high observed equivalent widths of the $\text{H}\beta$ and $\text{H}\alpha$ emission lines can not be

Table 4. Results of SED fitting

Parameter	SDSS		LBT			
(1)	(2)	(3)	(4)	(5)	(6)	(7)
$b = M_{\text{old}}/M_{\text{young}}$	1.7 [‡]	0.0 ^{‡‡}	8.0 ^{‡‡}	2.1 [‡]	0.0 ^{‡‡}	8.0 ^{‡‡}
t_{b} , Myr [*]	0.4	2.0	0.7	0.4	2.1	0.7
t_1 , Gyr ^{**}	0.8	...	9.7	1.4	...	9.7
t_2 , Gyr ^{**}	2.8	...	12.5	5.5	...	12.5
$\log M_{\text{young}}/M_{\odot}$ [†]	6.42	6.35	6.40	6.37	6.29	6.33
$\log M_{\text{old}}/M_{\odot}$ ^{††}	6.60	...	7.30	6.83	...	7.24
$\log M_{\star}/M_{\odot}$ ^{†††}	6.82	6.35	7.36	6.96	6.29	7.29

[‡]Best-fit value of the old-to-young stellar population mass ratio.

^{‡‡}Fixed value of b . The value $b = 0.0$ corresponds to the model with zero mass of the old stellar population. On the other hand, the value $b = 8.0$ corresponds to the model in which the old stellar population consists only of the least luminous stars in the age range between $t_1 \sim 10$ Gyr and $t_2 \sim 13$ Gyr.

^{*} t_{b} is the age of young stellar population.

^{**} $t_2 - t_1$ is the interval, in which the stellar population is formed.

[†] M_{young} is the mass of young stellar population.

^{††} M_{old} is the mass of old stellar population.

^{†††} M_{\star} is the total stellar mass derived from the extinction-corrected spectrum.

reproduced with our fitting procedure because of a too high contribution to the continuum by the emission of the old stellar population.

We note that, despite a wide range of b from 0 to 8 in the considered models, their best-fit SEDs are nearly indistinguishable, with only slightly different χ^2 . The adopted models with randomly varied b 's have the lowest values of χ^2 . Their SEDs are shown in Fig. 5.

The absolute SDSS g magnitude, corrected for the Milky Way extinction is $M_g = -16.39$ mag (Table 1). Thus, J2229+2725 is the second most luminous compact SFG known with $12 + \log O/H < 7.1$, after J1234+3901.

Adopting $M_{\star} = 10^{6.96} M_{\odot}$, we derive the very low mass-to-luminosity ratio M_{\star}/L_g of 0.0166 (in solar units) for J2229+2725. It is comparable to those of two other most metal-poor compact SFGs, J0811+4730 and J1234+3901 (Izotov et al. 2018a, 2019a). However, it is approximately one order of magnitude lower than the mass-to-luminosity ratio of another extremely metal-poor galaxy SFG AGC 198691 (Hirschauer et al. 2016), which contains a higher fraction of older stellar population (between 100 Myr and 1 Gyr), and up to two orders of magnitude lower than the mass-to-light ratios of the majority of compact SFGs in the SDSS which contain even more older stellar populations with ages between 100 Myr and 10 Gyr (see Fig. 6). Such a low value is consistent with the mass-to-luminosity ratio of a zero-age instantaneous burst, meaning that the contribution of older populations to the galaxy's luminosity is negligible compared to the starburst luminosity, at least, for the emission inside the spectroscopic aperture, in agreement with the galaxy's extremely high EW(H β).

6 LUMINOSITY – METALLICITY RELATION

It has been established (e. g. Izotov et al. 2018a, and references therein) that extremely metal-deficient galaxies with very active star formation deviate from the luminosity – metallicity relation defined by the bulk of the SDSS SFGs. The XMD galaxy J2229+2725 shows the same behavior, being too luminous for its oxygen abundance (Fig. 7). Oxygen

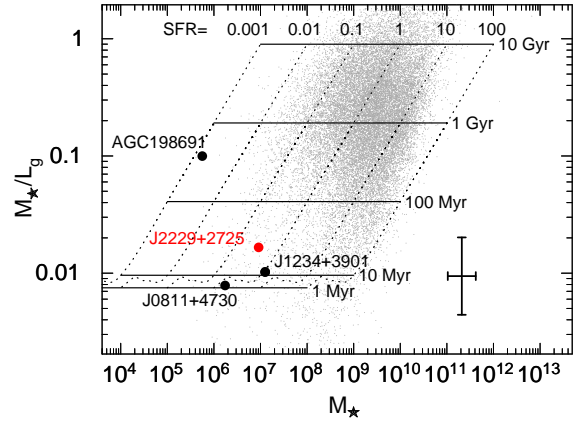


Figure 6. Relation between the stellar mass-to-luminosity ratio and the stellar mass of SFGs. All quantities are expressed in solar units. Selected lowest-metallicity SFGs J0811+4730, J1234+3901 and AGC 198691 with $12 + \log O/H \sim 7.0$ are represented by labelled black filled circles. The galaxy J2229+2725 is shown by a red filled circle. The error bars indicate the errors of M_{\star} and M_{\star}/L_g for that SFG. For comparison, compact SFGs from the SDSS DR16 with redshifts $z < 0.01$ (grey dots) are also shown. Dotted lines represent Starburst99 models with continuous star formation and a SFR varying from 0.001 to 100 $M_{\odot} \text{ yr}^{-1}$, during periods from the present to 10 Gyr, 1 Gyr, 100 Myr, 10 Myr, and 1 Myr in the past (horizontal solid lines). These models include the contribution of both the stellar and nebular continua.

abundances for all galaxies shown in Fig. 7 have been derived by the direct T_e method. In particular, only compact SFGs from the SDSS DR16 (grey dots) with an [O III] $\lambda 4363$ emission line detected in their spectra with an accuracy better than 20 per cent are included. The two galaxies with the lowest luminosities, Little Cub (Hsyu et al. 2017) and AGC 198691 (Hirschauer et al. 2016), deviate slightly from the relation by Berg et al. (2012) for relatively quiescent SFGs (crosses and dashed line in Fig. 7). On the other hand, all other lowest-metallicity SFGs, with higher luminosities, including J2229+2725, strongly deviate from the Berg et al. (2012) relation.

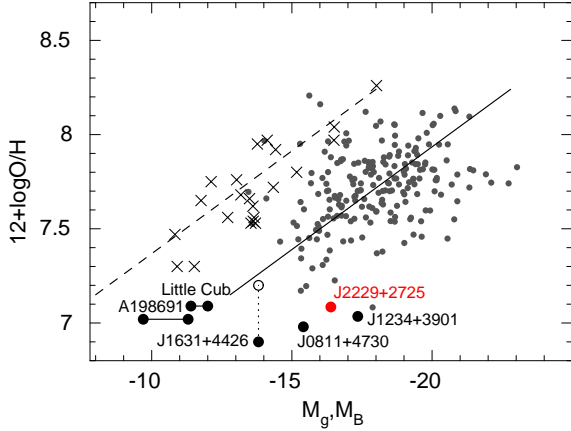


Figure 7. The oxygen abundance - absolute magnitude diagram. The most metal-poor galaxies (the same ones as in Fig. 4) are represented by filled and open circles. Low-luminosity galaxies are represented by crosses, with the fit to these data by Berg et al. (2012) shown by a dashed line. The solid line is the fit to the SDSS compact SFGs from DR16 with $EW(H\beta) \geq 200\text{\AA}$ and oxygen abundances derived by the direct T_e method (grey dots). This subsample of SDSS galaxies includes only compact galaxies with $[O\ III]\lambda 4363$ emission lines in their spectra, measured with errors less than 20 per cent of their fluxes. The vertical dotted line for J1631+4426 connects the locations of the galaxy with oxygen abundances derived by the direct T_e method (filled circle) and by the strong-line method (open circle, see Sect. 7). The horizontal lines connect the positions of the nearby galaxies AGC 198691 and Little Cub, calculated with two different distances.

It has been suggested e.g. by Izotov, Thuan & Guseva (2012) and Guseva et al. (2017) that these deviations can be explained by the enhanced brightnesses of the galaxies undergoing active star formation and they are higher for galaxies with high $EW(H\beta)$ and correspondingly with younger starburst age. In particular, Izotov et al. (2018a) have shown that the mass-to-luminosity ratio of the most extreme galaxies, like J2229+2725, are lower by a factor of more than 10 than typical ratios of SDSS galaxies. This difference translates to at least $\sim 2 - 3$ brighter magnitudes for the XMD starbursts and it can explain the offset of these galaxies from the relation for the bulk of compact SFGs from the SDSS (solid line in Fig. 7). On the other hand, SDSS compact galaxies are offset by ~ 3 mags to brighter magnitudes from the sample of quiescent dwarf galaxies studied by Berg et al. (2012), indicating that the luminosity of the latter galaxies is dominated not by young stellar populations in starburst regions, but by older stellar populations.

It has also been suggested that XMD galaxies have too low metallicities for their high luminosities. These low metallicities may have been caused by the infall of metal-poor gas from galactic halos (Ekta & Chengalur 2010).

7 MODIFIED STRONG-LINE METHOD FOR THE DETERMINATION OF OXYGEN ABUNDANCE

We have pointed out that J2229+2725 possesses the extraordinarily high O_{32} ratio of 53. We show in this section how such an object can be used to improve substantially

the calibration of the strong-line method to derive oxygen abundances in star-forming galaxies, including those with extreme excitation conditions.

The most reliable method for oxygen abundance determination is the direct method, but it requires the detection, with good accuracy, of the $[O\ III]\lambda 4363$ emission line for the electron temperature determination. However, most low-metallicity SFGs are intrinsically faint objects with a weak or undetected $[O\ III]\lambda 4363$ emission line, precluding a reliable oxygen abundance determination by the direct method. Many authors, including most recently e.g. Izotov et al. (2019b), have developed a so-called "strong-line method" with the use of strong oxygen lines, which is calibrated using high-quality observations of the most metal-poor galaxies with a well-detected $[O\ III]\lambda 4363$ emission line.

A common problem of the strong-line method is that it depends on several parameters. In particular, the method based on oxygen line intensities depends not only on the sum $R_{32} = I([O\ II]\lambda 3727 + [O\ III]\lambda 4959 + [O\ III]\lambda 5007)/I(H\beta)$, but also on the ionisation parameter. A good indicator of the ionisation parameter is the O_{32} ratio. The dependences of $12 + \log O/H$ on various combinations of oxygen line intensities are illustrated in Fig. 8, where we basically show the data of Izotov et al. (2019b), adding the two most recently discovered XMD galaxies, J1631+4426 by Kojima et al. (2020) and J2229+2725 discussed here. The oxygen abundances of all galaxies in Fig. 8 are derived by the direct method and the $[O\ III]\lambda 4363$ emission line is measured with errors less than 20 per cent in their fluxes. The $\log R_{23} - 12 + \log O/H$ diagram is shown in Fig. 8a. It is important that the data include objects with the largest O_{32} ratios, indicators of a very high ionisation parameter. The use of these galaxies allows us to better eliminate the dependence of the calibration relation on the ionisation parameter. The dispersion of data at the lowest-metallicity end of the diagram, with $12 + \log O/H \lesssim 7.3$, is relatively high and it is caused by different ionisation parameters in the galaxies. The most deviant objects are J2229+2725, with the highest O_{32} , and J1631+4426.

To minimise the data scatter, Izotov et al. (2019b) have proposed to use instead the diagram $\log(R_{23} - a_0 O_{32}) - (12 + \log O/H)$, with $a_0 = 0.080$ (Fig. 8b). The data in Fig. 8b, excluding the two deviant points J2229+2725 and J1631+4426, can be well fitted by the linear relation

$$12 + \log \frac{O}{H} = 0.950 \log(R_{23} - a_0 O_{32}) + 6.805. \quad (4)$$

shown by a solid line.

It is seen in Fig. 8b that the majority of the extremely low-metallicity SFGs follow tightly the relation Eq. 4. The scatter is small, much lower than that in Fig. 8a. Exceptions are the two SFGs mentioned above. One of them, J1631+4426, has a low $O_{32} = 3.41$ (Kojima et al. 2020), therefore its ionisation parameter correction is small and will not change much its location in Fig. 8b, compared to that in Fig. 8a. On the other hand, the ionisation parameter correction, based on Eq. 4, increases with increasing O_{32} , moving the galaxy to the left. Thus, for the SFG J2229+2725 with the highest $O_{32} = 53$, we find that $(R_{23} - a_0 O_{32})$ takes on a negative value, making Eq. 4 not applicable. The location of J2229+2725 shown in Fig. 8b corresponds to a slightly lower O_{32} of 50.7, at which $(R_{23} - a_0 O_{32})$ is still positive.

The large deviation of J2229+2725 from other galaxies

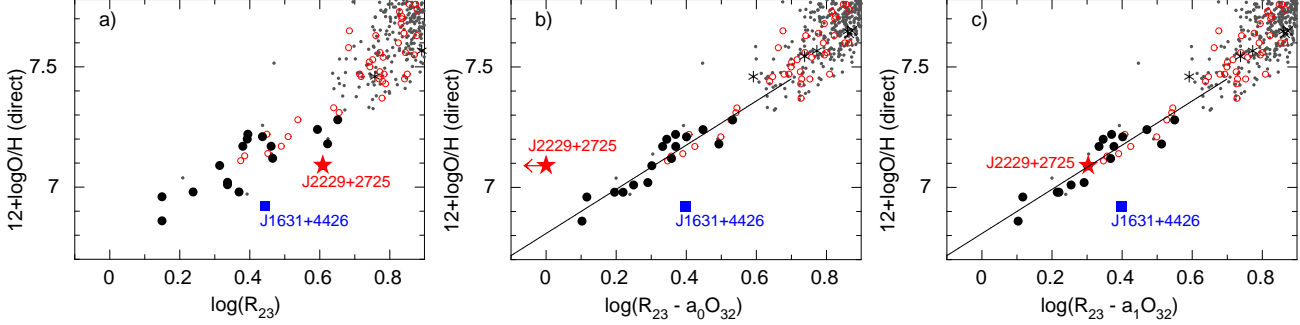


Figure 8. The **a)** $\log(R_{23}) - (12 + \log O/H)$, **b)** $\log(R_{23} - a_0 O_{32}) - (12 + \log O/H)$, and **c)** $\log(R_{23} - a_1 O_{32}) - (12 + \log O/H)$ relations, where $a_0 = 0.080$ (Izotov et al. 2019b) and $a_1 = 0.080 - 0.00078 O_{32}$ (this paper). In all these relations $12 + \log O/H$ is derived by the direct method, $R_{23} = ([O\ III]\lambda 4959 + \lambda 5007 + [O\ II]\lambda 3727)/H\beta$ and $O_{32} = [O\ III]\lambda 5007/[O\ II]\lambda 3727$. The galaxy J2229+2725 is shown by a red filled star, while J1631+4426 (Kojima et al. 2020) is represented by a blue filled square. Other lowest-metallicity SFGs from Izotov et al. (2018a), the galaxy Little Cub (Hsyu et al. 2017), the galaxy J1234+3901 from Izotov et al. (2019a) and the H II region DDO 68#7 (Annibali et al. 2019) are shown by filled circles. SFGs with the highest O_{32} ratios in the range $\sim 20 - 40$ (Izotov et al. 2017) are shown by asterisks. Samples of SFGs used for the He abundance determination (Izotov et al. 2014, and references therein) are shown by open circles. Grey dots represent SFGs at $z > 0.02$ from the SDSS, with the $[O\ II]\lambda 4363$ emission line measured with an accuracy better than 20 per cent. The solid lines in **b)** and **c)** are linear fits to the data with $\log(R_{23} - a_0 O_{32}) \leq 0.7$ and $\log(R_{23} - a_1 O_{32}) \leq 0.7$, respectively, and excluding J1631+4426.

thus suggests that Eq. 4 needs to be modified. The modification is found by minimising the scatter of galaxies, including J2229+2725. We found the relation

$$12 + \log \frac{O}{H} = 0.950 \log(R_{23} - a_1 O_{32}) + 6.805, \quad (5)$$

where $a_1 = 0.080 - 0.00078 O_{32}$. This relation is shown in Fig. 8c. It is seen that the SFG J2229+2725 follows very closely this relation.

On the other hand, the galaxy J1631+4426 remains an outlier. Kojima et al. (2020) have derived $12 + \log O/H = 6.90 \pm 0.03$ for this galaxy, making it the most metal-poor SFG known. However, this very low oxygen abundance is not supported by Eq. 5. Using this equation we derive $12 + \log O/H = 7.18$ for J1631+4426, in full agreement with the value derived by Kojima et al. (2020) with the use of strong-line calibration. If so, J1631+4426 can not be considered as the most metal-deficient nearby SFG known. However, new high quality observations of J1631+4426 are needed to confirm this conclusion.

Eq. 5 can be used to search for extremely low-metallicity galaxies with oxygen abundances extending to values $12 + \log O/H < 7.0$, a range where other methods are not applicable because of the weakness of the emission lines. In addition, it can be used to verify the abundances derived by the direct method.

8 CONCLUSIONS

We present Large Binocular Telescope (LBT)/Multi-Object Dual Spectrograph (MODS) spectrophotometric observations of the compact star-forming galaxy (SFG) J2229+2725, selected from the Data Release 16 (DR16) of the Sloan Digital Sky Survey (SDSS). This local SFG possesses extraordinary properties (in particular a very low metallicity and an extremely high O_{32} ratio), which makes it stand apart from other galaxies. LBT observations have been supplemented by medium-resolution spectroscopy with the Dual Imaging Spectrograph (DIS) mounted on the 3.5

meter telescope of the Apache Point Observatory (APO). Our main results are as follows.

1. The emission-line spectrum of J2229+2725, with a stellar mass of $9.1 \times 10^6 M_{\odot}$ and an absolute SDSS g -band magnitude of -16.39 mag, originates from a very dense ($N_e(S\ II) = 1000\text{ cm}^{-3}$) and hot ($T_e(O\ III) = 24800\text{ K}$) ionised gas. The detection of the He II $\lambda 4686$ emission line with the flux ratio $I(\text{He II } \lambda 4686)/I(H\beta)$ of ~ 0.021 indicates the presence of hard ionising radiation. The oxygen abundance in J2229+2725 is $12 + \log O/H = 7.085 \pm 0.031$, one of the lowest for nearby SFGs.

2. The rest-frame equivalent width $EW(H\beta)$ of the $H\beta$ emission line of 577 \AA in the J2229+2725 spectrum is the highest measured so far in SFGs. The mass-to-luminosity ratio M_*/L_g in J2229+2725 of ~ 0.017 in solar units is extremely low. Both the extremely high $EW(H\beta)$ and extremely low M_*/L_g indicate that the J2229+2725 emission is strongly dominated by a very young stellar population with an age $\lesssim 2$ Myr. These properties are similar to those of the two most metal-deficient SFGs known, J0811+4730 and J1234+3901 (Izotov et al. 2018a, 2019b).

3. The $O_{32} = I([O\ III]\lambda 5007)/I([O\ II]\lambda 3727)$ flux ratio of ~ 53 in J2229+2725 is extremely high. It is the highest ever measured for low-metallicity SFGs. These properties together with the extremely high rest-frame equivalent width $EW(H\beta)$ of the $H\beta$ emission line and the very dense H II region imply that this galaxy might be at a very young stage of its formation. If so, then J2229+2725 is one of the best local counterparts of young high-redshift dwarf SFGs.

4. J2229+2725 strongly deviates from the luminosity-metallicity relation defined by the bulk of compact SDSS SFGs. It is ~ 2.5 times more metal-poor for its SDSS g -band absolute magnitude.

5. A medium resolution spectrum of J2229+2725 obtained with the Double Imaging Spectrograph mounted on the 3.5 meter Apache Point Observatory (APO) telescope shows that the ionised gas kinematics are dominated by macroscopic turbulent motions with a velocity dispersion of

31.6 km s⁻¹, with no evident sign of merging or asymmetric infall or outflow.

6. The extremely high O₃₂ ratio in J2229+2725 allowed us to use the latter to improve the calibration of the strong-line method of oxygen abundance determination in extremely low-metallicity SFGs (with 12 + logO/H < 7.45), which is based on the fluxes of strong nebular emission lines [O II]λ3727 and [O III]λ4959+λ5007 emission lines.

7. The proposed strong-line method can be used to search for SFGs at the extreme end of oxygen abundances 12 + logO/H < 7.0, where other methods, including the direct T_e method, can not be applied because of the weakness of emission lines. This method can also be applied to verify oxygen abundances derived by the direct T_e method. In particular, using our new calibration of the strong-line method, we find that the oxygen abundance for the galaxy J1631+4426 is 0.28 dex higher than the value 12 + logO/H = 6.90±0.03 derived by Kojima et al. (2020) using the direct T_e method, but it is consistent with their value derived using the strong-line method.

ACKNOWLEDGEMENTS

We are grateful to the anonymous referee for useful comments on the manuscript. Y.I.I. and N.G.G. acknowledge support from the National Academy of Sciences of Ukraine by its priority project No. 0120U100935 “Fundamental properties of the matter in the relativistic collisions of nuclei and in the early Universe”. Funding for the Sloan Digital Sky Survey IV has been provided by the Alfred P. Sloan Foundation, the U.S. Department of Energy Office of Science, and the Participating Institutions. SDSS-IV acknowledges support and resources from the Center for High-Performance Computing at the University of Utah. The SDSS web site is www.sdss.org. SDSS-IV is managed by the Astrophysical Research Consortium for the Participating Institutions of the SDSS Collaboration. This research has made use of the NASA/IPAC Extragalactic Database (NED), which is operated by the Jet Propulsion Laboratory, California Institute of Technology, under contract with the National Aeronautics and Space Administration.

DATA AVAILABILITY

The data underlying this article will be shared on reasonable request to the corresponding author.

REFERENCES

- Ahumada R. et al., 2020, ApJS, 249, 1
 Annibali F. et al., 2019, MNRAS, 482, 3892
 Berg D. A. et al., 2012, ApJ, 754, 98
 Bouwens R. J., Illingworth G. D., Oesch P. A., Caruana J., Holwerda B., Smit R., Wilkins S., 2015, ApJ, 811, 140
 Ekta B, Chengalur J. N., 2010, MNRAS, 406, 1238
 Filippenko A. V., 1982, PASP, 94, 715
 Girardi L., Bressan A., Bertelli G., Chiosi C., 2000, A&AS, 141, 371
 Guseva N. G., Izotov Y. I., Fricke K. J., Henkel C., 2017, A&A, 599, A65
 Hirschauer A. S. et al., 2016, ApJ, 822, 108
 Hsyu T., Cooke R. J., Prochaska J. X., Bolte M., 2017, ApJ, 845, L22
 Izotov Y. I., Thuan T. X., Lipovetsky V. A., 1994, ApJ, 435, 647
 Izotov Y. I., Stasińska G., Meynet G., Guseva N. G., Thuan T. X., 2006, A&A, 448, 955
 Izotov Y. I., Guseva N. G., Fricke K. J., Papaderos P., 2009, A&A, 503, 61
 Izotov Y. I., Thuan T. X., Guseva N. G., 2012, A&A, 546, 122
 Izotov Y. I., Guseva N. G., Fricke K. J., Henkel C., 2014, A&A, 561, 33
 Izotov Y. I., Orlitová I., Schaerer D., Thuan T. X., Verhamme A., Guseva N. G., Worseck G., 2016a, Nature, 529, 178
 Izotov Y. I., Schaerer D., Thuan, T. X., Worseck G., Guseva N. G., Orlitová I., Verhamme A., 2016b, MNRAS, 461, 3683
 Izotov Y. I., Thuan T. X., Guseva N. G., 2017, MNRAS, 471, 548
 Izotov Y. I., Thuan T. X., Guseva N. G., Liss S. E., 2018a, MNRAS, 473, 1956
 Izotov Y. I., Schaerer D., Worseck G., Guseva N. G., Thuan, T. X., Verhamme A., Orlitová I., Fricke K. J., 2018b, MNRAS, 474, 4514
 Izotov Y. I., Worseck G., Schaerer D., Guseva N. G., Thuan, T. X., Fricke K. J., Verhamme A., Orlitová I., 2018c, MNRAS, 478, 4851
 Izotov Y. I., Thuan T. X., Guseva N. G., 2019a, MNRAS, 483, 5491
 Izotov Y. I., Guseva N. G., Fricke K. J., Henkel C., 2019b, A&A, 623, 40
 Izotov Y. I., Schaerer D., Worseck G., Verhamme A., Guseva N. G., Thuan T. X., Orlitová I., Fricke K. J., 2020, MNRAS, 491, 468
 Kennicutt R. C., Jr., 1998, Ann.Rev.Astron.Astrophys., 36, 189
 Kojima T. et al., 2020, ApJ, 898, 142
 Leitherer C. et al., 1999, ApJS, 123, 3
 Lejeune T., Buser R., Cuisinier F., 1997, A&AS, 125, 229
 Mitra S., Ferrara A., Choudhury T. R., 2013, MNRAS, 428, L1
 Ouchi M. et al., 2009, ApJ, 706, 1136
 Planck Collaboration XVI, 2014, A&A, 571, 16
 Salpeter E. E., 1955, ApJ, 121, 161
 Storey P. J., Hummer D. G., 1995, MNRAS, 272, 41
 Wise J. H., Cen R., 2009, ApJ, 693, 984
 Yajima H., Choi J.-H., Nagamine K., 2011, MNRAS, 412, 411

This paper has been typeset from a T_EX/L^AT_EX file prepared by the author.